

This is an Open Access document downloaded from ORCA, Cardiff University's institutional repository: <https://orca.cardiff.ac.uk/id/eprint/151688/>

This is the author's version of a work that was submitted to / accepted for publication.

Citation for final published version:

Yu, Kaiqi, Alves, Tiago M. , Li, Wei, Li, Shuang, Li, Jian, Zhao, Fang, Wu, Shiguo and Zhan, Wenhuan 2022. The role of bottom currents on the morphological development around a drowned carbonate platform, NW South China Sea. *Journal of Ocean University of China: Oceanic and Coastal Sea Research* 21 (4) , 801–812.  
10.1007/s11802-022-5020-4

Publishers page: <http://dx.doi.org/10.1007/s11802-022-5020-4>

Please note:

Changes made as a result of publishing processes such as copy-editing, formatting and page numbers may not be reflected in this version. For the definitive version of this publication, please refer to the published source. You are advised to consult the publisher's version if you wish to cite this paper.

This version is being made available in accordance with publisher policies. See <http://orca.cf.ac.uk/policies.html> for usage policies. Copyright and moral rights for publications made available in ORCA are retained by the copyright holders.



# **The role of bottom currents on the morphological development around a drowned carbonate platform, NW South China Sea**

Yu Kaiqi<sup>1,2,3</sup>, Alves Tiago M.<sup>4</sup>, Li Wei<sup>1,2,3</sup>, Li Shuang<sup>1,2,3</sup>, Li Jian<sup>1,2,3</sup>, Zhao Fang<sup>1,2,3</sup>, Wu  
Shiguo<sup>3,5</sup>, Zhan Wenhuan<sup>1,2,3</sup>

1) CAS Key Laboratory of Ocean and Marginal Sea Geology, South China Sea Institute of Oceanology, Chinese  
Academy of Sciences, Guangzhou 510301, China

2) Southern Marine Science and Engineering Guangdong Laboratory (Guangzhou), Guangzhou 511458, China

3) University of Chinese Academy of Sciences, Beijing 100049, China

4) 3D Seismic Laboratory, School of Earth and Environmental Sciences, Cardiff University, Cardiff CF10 3AT,  
United Kingdom

5) Institute of Deep-Sea Science and Engineering, Chinese Academy of Sciences, Sanya 572000, China

**Abstract:** The seafloor around carbonate platforms is largely shaped and modified by  
downslope processes. However, the role of alongslope processes, including bottom currents,  
on the morphological development of carbonate platforms remains poorly understood. Here,  
we use high-resolution multibeam bathymetric data and two-dimensional seismic profiles to  
investigate the detailed sea-floor morphology around the Zhongjianbei carbonate platform  
(ZCP) in the northwest South China Sea. A series of depositional bodies and erosional  
channels are identified to the south of the ZCP and are interpreted as contourite drifts and  
channels resulted from the interaction between bottom currents and bathymetric features. In  
addition, active fluid seepages have led to the formation of widespread pockmarks on the  
seafloor. Importantly, the contourite channels and widespread pockmarks also show a close

24 relationship in their distribution. We propose that the contourite channels around the ZCP are  
25 evolved from the coalescence of pockmarks under the persistent erosion of bottom currents.  
26 Based on the morphological analysis, we reconstruct the past bottom-current pathways  
27 around the ZCP that are parallel to the platform slopes and heading to the south. This study  
28 provides new insights into the formation of complex bathymetry and helps understanding  
29 how bottom currents and active fluid seepages can influence the morphological development  
30 around carbonate platforms.

31

32 **Keywords:** carbonate platform; seafloor morphology; contourite channels; bottom currents;  
33 fluid seepages; South China Sea.

34

## 35 **1. Introduction**

36 Carbonate platforms are formed in the photic zone and occur widely on continental margins  
37 and abyssal plains of tropical seas (Betzler et al., 1995; Wilson et al., 1998; Eberli et al.,  
38 2010; Mulder et al., 2012; Lüdmann et al., 2013; Shao et al., 2017; Betzler and Eberli, 2019).  
39 They form important carbonate factories in source-to-sink systems, and thus feed abundant  
40 sediments to surrounding sedimentary basins (Merino-Tomé et al., 2012; Counts et al., 2018;  
41 Michel et al., 2019). In addition, the development of carbonate platforms significantly  
42 changes the surrounding seafloor morphology, and thereby influences the regional  
43 sedimentary and oceanographic dynamics (Mulder et al., 2017; Wunsch et al., 2017; Nolting  
44 et al., 2018; Principaud et al., 2018).

45 Due to their importance in oceanography, sedimentology and submarine geohazards, the  
46 morphological development of carbonate platforms has drawn increasing attention in recent  
47 years (Menier et al., 2014; Purkis et al., 2014; Prat et al., 2016). Studies have shown that

48 downslope and along-slope processes are two of the most important mechanisms shaping the  
49 seafloor around carbonate platforms (Mulder et al., 2012; Principaud et al., 2017; Eberli et  
50 al., 2019). Downslope processes include submarine mass wasting, slope failure and turbidity  
51 currents, which form particular seafloor bedforms such as sediment waves, slide scars, creep,  
52 submarine channels and gullies (Dowdeswell et al., 2006; Heinio and Davies, 2009; Li et al.,  
53 2016, 2018). Bathymetric features formed by downslope processes have been investigated in  
54 many regions such as the Mozambique Channel (Courgeon et al., 2016; Counts et al., 2018),  
55 Australian North West Shelf (Rankey, 2017; Rinke-Hardekopf et al., 2018) and Little and  
56 Great Bahama Bank (Mulder et al., 2017). Together with downslope processes, along-slope  
57 bottom currents can also significantly shape and modify the seafloor morphology, producing  
58 erosional and depositional bedforms (García et al., 2009; Stow et al., 2009; Rebesco et al.,  
59 2014; Miramontes et al., 2019a). In recent years, an increasing number of articles has  
60 documented the importance of bottom currents on the flanks of carbonate platforms in the  
61 Maldives (Lüdmann et al., 2013), Bahamian archipelago (Mulder et al., 2019) and South  
62 China Sea (Shao et al., 2017). They have proved that bottom currents redistribute sediments  
63 shed by the carbonate platforms and erode their flanks to generate sediment drifts, moats,  
64 contourite channels and furrows. However, compared to the downslope processes around  
65 carbonate platforms, the importance of alongslope currents in such platforms is still poorly  
66 understood.

67 Due to the favorable latitude, oceanographic and tectonic setting of the northwest South  
68 China Sea, a large number of carbonate platforms have developed in this region since the  
69 early Miocene (Wu et al., 2014, 2016; Gao et al., 2019). The bathymetry of the northwest  
70 South China Sea has largely influenced the oceanographic setting in this region, especially  
71 the pathways of bottom currents (Chen et al., 2016; Yin et al., 2021). This study focuses on  
72 investigating the role of bottom currents on the morphological development around an

73 isolated, drowned carbonate platform, the Zhongjianbei carbonate platform (ZCP). High-  
74 resolution multibeam bathymetric data and two-dimensional (2D) seismic lines are used to: 1)  
75 characterize the bathymetry around the ZCP and evidence for the presence of bottom-current  
76 activity; 2) reconstruct past bottom-current pathways around the ZCP; and 3) propose a  
77 representative model explaining the complex seafloor bedforms observed around the ZCP  
78 and other carbonate platforms.

79

## 80 **2. Regional Setting**

81

### 82 *2.1 Geological Background*

83 The South China Sea is the largest ( $3.5 \times 10^6$  km<sup>2</sup>) and deepest (> 5000 m) marginal sea in the  
84 western Pacific Ocean (Wang and Wang, 1990). The northwest South China Sea was formed  
85 after the late Cretaceous by distinct tectonic activities: continental rifting, continental  
86 breakup, and post-rift tectonism (Zhou et al., 1995; Li et al., 2015a; Lei et al., 2020; Zhang et  
87 al., 2021). It comprises several Cenozoic rift basins such as the Pearl River Mouth,  
88 Qiongdongnan, Yinggehai and Zhongjiannan Basins (Zhao et al., 2020). In the Paleocene,  
89 hyperextension led to the formation of a regional basement high in the northwest South China  
90 Sea, later developing as a shallow platform on which the Xisha Islands developed  
91 (Tapponnier et al., 1990; Li et al., 2015a). The northwest South China Sea entered a phase of  
92 thermal subsidence in the early Miocene (Wu et al., 2009), with post-rift tectonics promoting  
93 the growth of carbonate platforms (Wu et al., 2014; Zhu et al., 2017).

94 Carbonate platforms in the northwest South China Sea mainly occur above the Xisha and  
95 Guangle highs, and are separated into two distinct groups by the Zhongjian canyon (Lu et al.,  
96 2018; Gao et al., 2019). The Zhongjianbei carbonate platform (ZCP), the focus of this study,

97 is an isolated and drowned carbonate platform located to the north-east of the Guangle high  
98 and southwest of the Zhongjian canyon, at a water depth between 350 and 1200 m (Figs.1, 2  
99 and 3). The Neogene and Quaternary stratigraphy in the surrounding region of the ZCP is  
100 divided into five formations: the Ledong, Yinggehai, Huangliu, Meishan, and Sanya  
101 formations (Gao et al., 2019). Based on regional correlations with adjacent basins (Li et al.,  
102 2015b; Lu et al., 2018; Gao et al., 2019), four seismic horizons, T30, T40, T50 and T60, have  
103 been identified in the seismic profiles, corresponding to the bottom interfaces of Pliocene,  
104 late Miocene, middle Miocene and early Miocene strata, respectively (Figs.1C, 4 – 6).

105

## 106 *2.2 Oceanography*

107 The South China Sea is a semi-enclosed marginal sea connected to the Pacific Ocean via the  
108 Luzon Strait (Liu et al., 2008). Four major water masses are identified: surface, intermediate,  
109 deep and bottom water (Tian et al., 2006; Quan et al., 2016; Yin et al., 2021). Surface water  
110 moves cyclonically between 0 and 750 m at a speed of up to 100 cm s<sup>-1</sup>, whereas the South  
111 China Sea intermediate water circulates anticyclonically between 750 and 1500 m water  
112 depth at a speed of 5 – 15 cm s<sup>-1</sup> (Quan et al., 2016). Deep water flows at a depth of 1500 to  
113 2200 m, while bottom water occurs below 2200 m. Both deep and bottom waters have an  
114 average speed lower than 5 cm s<sup>-1</sup> (Zeng et al., 2016; Zhu et al., 2019).

115 The South China Sea was isolated from the North Pacific subtropical gyre in the late Miocene  
116 due to the formation of the Luzon Strait (Tian et al., 2006). This event resulted in a major  
117 palaeo-oceanographic shift, which promoted the anti-clockwise flow of surface water masses  
118 in the Northwest South China Sea (Yin et al., 2021). Present day surface water circulation is  
119 dominated by a Western Boundary Current flowing southward (Fig.1B). Flowing through the  
120 study area all year, this current can reach a depth of about 600 m, a maximum instantaneous

121 velocity of more than 1 cm s<sup>-1</sup> and play a key role in the distribution of mass, energy and  
122 heat in the South China Sea (Quan et al., 2016). High-resolution ocean circulation models for  
123 the western Pacific and northern Indian Oceans record a predominant anti-clockwise  
124 circulation for intermediate water masses of the South China Sea (Liang et al., 2019).

125

### 126 **3. Data and Methods**

127 This study is based on the interpretation of high-resolution multibeam bathymetric data and  
128 two-dimensional (2D) multi-channel seismic reflection profiles. The multibeam bathymetric  
129 data were acquired by a SeaBeam 2112 system in 2008. The horizontal and vertical  
130 resolution of the bathymetric data are 100 m (cell size) and 3 m (3% of the water depth). The  
131 bathymetric data were imported and analyzed in Global Mapper® to investigate the  
132 bathymetry around the ZCP in detail.

133 The two-dimensional (2D) seismic reflection data were acquired by the China National  
134 Petroleum Company (CNPC) in 2005 and processed by using the software package Pro-Max  
135 from Landmark®. Seismic data were migrated with a common midpoint (CMP) spacing of  
136 12.5 m, and a main frequency bandwidth of 30 Hz to 45 Hz, for a main frequency of 35 Hz.  
137 Vertical resolution for these seismic data approaches 25 m. The 2D seismic reflection data  
138 were interpreted by using Landmark®.

139 The multibeam bathymetric data in this study covers more than 3000 km<sup>2</sup> (Figs.1, 2 and 3).  
140 We have specifically investigated the dimension, incision depth, and scale of seafloor  
141 features formed around the ZCP. Moreover, based on the 2D seismic profiles crossing  
142 erosional features in the study area, we were able to investigate subsurface structures and  
143 their relationship with seafloor features (Figs.3 – 5). Changes in seismic attributes (e.g.,

144 amplitude, polarity, uniformity and continuity) were used to interpret faults, palaeo-  
145 pockmark, palaeo-channel and fluid-escape structures.

146

## 147 **4. Results**

148 Based on the analysis of multibeam bathymetric data and two-dimensional seismic profiles,  
149 we have identified several seafloor morphological features and subsurface structures.

150

### 151 *4.1 Seafloor morphology*

152 The ZCP has a flat top and three flanking slopes facing the northeast, southeast and southwest  
153 (Fig.1B). On its southern flanks, the seafloor predominantly comprises alongslope  
154 morphological features such as channels and elongated depressions (Figs.2 and 3).  
155 Alongslope morphological features are absent on the northeast flank of the ZCP; they are  
156 replaced by base-of-slope sediments (Fig.1B).

157

#### 158 *4.1.1 Seafloor erosional features*

159 Erosional features are the most remarkable and dominant alongslope morphological features  
160 on the southern flanks of the ZCP (Figs.2 and 3). They are parallel and oriented in a similar  
161 direction to the slopes bordering the ZCP. They show a relatively constant spacing of about  
162 1.5 km and occur in combination with elongated and mounded depositional bodies (Figs.2  
163 and 3). Topographic profiles crossing these erosional features show a similar ‘U-shaped’  
164 geometry (Figs.2D, 2E, 3C and 3D). Their width ranges from 0.5 to 2 km, and their  
165 maximum depth of incision is 160 m. The length of these erosional features decreases to the  
166 south, with maximum and minimum lengths of 20 km and 7 km, respectively. Two channel-



167 like erosional features occur on the bottom of southwest and south-east slopes of the ZCP,  
168 presenting smoother thalwegs and shallower incision depths than other channel-like erosional  
169 features in the study area (Figs.2 and 3).

170

#### 171 *4.1.2 Seafloor depressions*

172 A large number of depressions are identified on the southern flanks of the ZCP, close to the  
173 previous erosional features (Figs.2 and 3). These depressions are crescent, elongated and  
174 circular in plan-view. They are 50- to 100-m deep with a diameter ranging from hundreds of  
175 meters to more than 1 km. Some of these isolated depressions are observed at the ends of  
176 channel-like erosional features (e.g., C1 and C2; Fig.2C). In addition, several elongated  
177 depressions forming distinct trails are also extended in the direction of channel-like erosional  
178 features (e.g., C3 and C7; Figs.2C and 3B). The elongated depressions, when distributed in  
179 trails, have a similar morphology to the channel-like erosional features, especially when their  
180 width and incision depth are considered (Figs.2 and 3). Furthermore, the relics of elongated  
181 depressions exist at the bases of channel-like erosional features (e.g., C6 and C7; Fig.3B).

182

#### 183 *4.2 Subsurface Structures*

184 Mounded depositional bodies, palaeo-depressions, palaeo-erosional features, pipe and  
185 chimney structures, mainly occur in strata younger than Horizon T50 (15.5 Myr). They  
186 mainly occur to the south of the ZCP (Figs.4 – 6).

187

##### 188 *4.2.1 Mounded depositional bodies*

189 Mounded depositional bodies are observed above Horizon T30 (5.5 Myr) on the southern  
190 flanks of the ZCP (Figs.4 and 5). The width of these depositional bodies ranges from 2 to 3  
191 km and their thickness reaches more than 300 m (Figs.4 and 5). They are characterised by  
192 continuous, parallel and convex internal seismic reflections with low to medium amplitude.  
193 The mounds are truncated by erosional features and pinch out towards the ZCP (Figs.4A, 4B,  
194 5A and 5D).

195

#### 196 *4.2.2 Palaeo-depressions and paleo-erosional features*

197 Multiple palaeo-depressions and palaeo-erosional features have been identified in strata  
198 above Horizon T40 (10.5 Myr) (Figs.4 – 6). The lower boundaries of them are continuous  
199 and concave seismic reflections with high amplitude, and some of them coincide with  
200 Horizon T30 (5.5 Myr) (Figs.5B and 5C). Palaeo-depressions are filled with parallel,  
201 continuous strata. Chaotic strata occur at their bases (Figs.5A and 5B).

202 Similar to the palaeo-depressions described above, other palaeo-erosional features are imaged  
203 as concave seismic reflections with medium to high amplitude that truncate the surrounding  
204 strata (Figs.4 – 6). Palaeo-erosional features usually show a ‘U-shaped’ geometry in cross-  
205 section and correlate well with other channel-like erosional features on the seafloor (Figs.5D  
206 and 5E). Palaeo-erosional features clearly migrate laterally, as shown by the vertical  
207 superposition of multiple palaeo-erosional features (Figs.5C, 5D and 5E).

208

#### 209 *4.2.3 Fluid pipes and chimneys*

210 Fluid pipe and chimney structures are observed on the south flanks of the ZCP, but are rarely  
211 identified on the north flank of the ZCP (Figs.4 – 6). They form cones or pipes in seismic

212 images, and their internal seismic reflections are chaotic with low to medium amplitude  
213 (Figs.4C, 4D, 5B, 5C and 5E). These structures, rooted in strata below Horizons T30 or T40,  
214 develop vertically into younger strata (Figs.4 and 5). Some end at the bases of the palaeo-  
215 depressions or palaeo-erosional features, while other are linked with surface depressions  
216 (Figs.4B and 5A).

217

## 218 **5. Discussion**

219

### 220 *5.1 Evidence for the occurrence of bottom currents*

221 A series of channel-like erosional features and elongated depositional bodies are identified on  
222 the southern flanks of the ZCP. Generally, these erosional features and depositional bodies  
223 are distributed in an alongslope direction, indicating a common formation mechanism.

224 Channel-like erosional features to the south of the ZCP have the following morphological  
225 characteristics (Figs.2 and 3): 1) they are parallel to the regional contours and the strikes of  
226 platform slopes; 2) they present ‘U-shaped’ geometries in cross-section, with the average  
227 width of 1.5 km and the incision depth of 120 m; 3) they reveal a constant spacing of 1.2 km.  
228 Based on these observations, downslope processes (e.g., mass wasting or turbidity currents)  
229 can be excluded as the origin for these channels. We propose that these channel-like erosional  
230 features comprise contourite channels, similar to the features documented in the western  
231 Mediterranean (de Weger et al., 2020), Gulf of Cadiz (García et al., 2009) and western South  
232 China Sea (Yin et al., 2021).

233 Depositional bodies along the flanks of the ZCP are characterised by their variable mounded  
234 geometries, especially their distinctly elongated and mounded shape (Figs.2 and 3). Their

235 internal seismic reflections are smooth, parallel and continuous, often interbedded with  
236 transparent zones (Figs.4 and 5). Internal seismic reflections thin out towards the platform  
237 flanks and are truncated by erosional channels away from the ZCP. They are also separated  
238 from the platform by an alongslope erosional channel (Figs.4 and 5).

239 Our interpretation provides the robust evidence for discrete contourite drifts along the flanks  
240 of the ZCP, which were accumulated by the persistent action of bottom currents. The two  
241 channels that are closest to the southern flanks of the ZCP, separate the contourite drifts from  
242 the carbonate platform, and are therefore considered as erosional moats (Figs.2 – 5). Similar  
243 contourite drifts, combined with erosional moats formed by alongslope processes, are  
244 documented in regions such as the Danish Basin (Surlyk and Lykke-Andersen, 2007),  
245 Western Mediterranean Sea (Miramontes et al., 2019a), Bahamian Archipelago (Mulder et  
246 al., 2019), SE Brazil (Alves, 2010) and Great Australian Bight (Jackson et al., 2019).  
247 Furthermore, palaeo-depressions and associated palaeo-erosional features identified in the  
248 seismic profiles may be the residue of palaeo-pockmarks and palaeo-channels, suggesting the  
249 important activity of bottom currents in the past (Yin et al., 2021).

250

## 251 *5.2 Reconstructing the pathways of bottom currents around the ZCP*

252 Previous studies have used multiple methods to reconstruct the pathways of bottom-currents,  
253 including: a) numerical simulations (Chen et al., 2016; Miramontes et al., 2019a), b) palaeo-  
254 bathymetric analyses (de Weger et al., 2020) and, c) in situ current measurements via  
255 moorings and landers (Miramontes et al., 2019b). In addition, the concept of space-for-time  
256 substitution – referring to the understanding of long-term landform development by  
257 comparing similar landforms of different ages or at different stages of evolution – has been  
258 previously used to reconstruct the evolution of submarine channels (Micallef et al., 2014). In

259 particular, the direction and relative velocity of bottom currents can be inferred from the  
260 trend, depth and asymmetry of contourite channels (García et al., 2009; Stow et al., 2009).

261 Here, we utilize the concept of space-for-time substitution to investigate the development of  
262 contourite channels around the ZCP, and thereby reconstruct the pathways of palaeo-bottom  
263 currents. Seafloor pockmarks occur in trails that co-exist with the contourite channels  
264 observed around the ZCP (Figs.2 and 3). Kilhams et al. (2011) have demonstrated that trails  
265 of pockmarks can coalesce to form furrows, or immature channels under the continuous  
266 erosion of bottom currents. We therefore propose that the contourite channels around the ZCP  
267 are also developed from pockmark trails (Figs.2 and 3); they are interpreted as leading to the  
268 inception of contourite channels. Under the erosion of bottom currents, some of the  
269 pockmarks coalesced to form immature channels, which are characterized by rugged  
270 thalwegs (e.g., channels C3, C6 and C7; Figs.2 and 3). Immature channels subsequently  
271 evolved into mature channels under the further erosion of bottom currents. We also propose  
272 that the direction of a contourite channel indicates both the original strike of pockmarks in a  
273 trail and the flow direction of bottom currents. This is the reason why the contourite channels  
274 along the flanks of the ZCP developed towards the southeast and southwest, respectively  
275 (Fig.7). Bottom-current should flow to the direction which these contourite channels  
276 developed towards, from north of the ZCP to the south (Fig.7). Seafloor bathymetry also  
277 greatly impact the hydrodynamics of bottom currents (Hernández-Molina et al., 2006; de  
278 Castro et al., 2020): The ZCP splits the bottom currents into two branches and intensified the  
279 erosion to the slope close to the base, generating contourite channels along the southeast and  
280 southwest flanks of the ZCP (Fig.7).

281 Palaeo-erosional features indicate that palaeo-channels were formed in upper Miocene strata  
282 (Figs.4 – 6). However, on the northeast flank of the ZCP, the palaeo-bottom currents  
283 gradually diminished in strength after the Late Miocene and left no erosional features on the

284 modern sea-floor (Fig.6). The identification of palaeo-pockmarks and palaeo-channels on the  
285 seismic profiles indicates that bottom currents were already active in the late Miocene (5.5  
286 Myr), reshaping pre-existing pockmarks and contributing to the formation of palaeo-channels  
287 (Figs.4 and 5). Unfortunately, due to the lack of three-dimensional seismic data, it is  
288 impossible to characterise the overall morphology of palaeo-pockmarks and paleo-channels,  
289 particularly when the time-dependent morphological evolution of palaeo-pockmarks towards  
290 contourite channels is considered. Based on the interpreted seismic data, we propose that  
291 the change from pockmarks to contourite channels occurred after the late Miocene (5.5 Myr),  
292 as pockmarks and contourite channels on the modern seafloor reveal such change – from  
293 pockmarks to channels – is ongoing (Figs.2, 3 and 7).

294

### 295 *5.3 Interaction between bottom currents and fluid seepages*

296 The morphology around carbonate platforms can be significantly shaped and modified by  
297 alongslope processes (bottom currents) via the formation of moats, contourite channels and  
298 drifts (Lüdmann et al., 2013; Betzler and Eberli, 2019; Eberli et al., 2019; Mulder et al.,  
299 2019). However, the complex morphology around the ZCP is marked by large numbers of  
300 parallel contourite channels, which occur in combination with widespread pockmarks (Figs.2  
301 and 3), a pattern rarely observed in other parts of the world.

302 Based on the interpretation of high-resolution seismic reflection data, Gao et al. (2019)  
303 demonstrated that late Cenozoic magmatism led to the formation of hydrothermal systems  
304 and the build-up of local overpressures, both responsible for active fluid seepages around the  
305 Xisha Islands. Fluid escape structures are widely identified on the seismic profiles on the  
306 flanks of the ZCP (Figs.4 and 5). Around the ZCP, fluid escape structures rooted in middle to  
307 upper Miocene strata have been identified beneath the interpreted channels and pockmarks

308 (Figs.4 and 5). These structures, imaged in seismic data as columnar features with dimmed  
309 internal reflections due to local amplitude and velocity anomalies, mark the pathways for  
310 focused fluid venting that generated seafloor pockmarks (Pilcher and Argent, 2007; León et  
311 al., 2010; Cartwright and Santamarina, 2015; Bertoni et al., 2017; Velayatham et al., 2018).  
312 The local seafloor relief produced by the pockmarks led to the enhancement of bottom-  
313 current erosion in their leeward and/or windward side and, as a result, pockmarks become  
314 elongated along the flowing direction of bottom currents (Andresen et al., 2008; Kilhams et  
315 al., 2011).

316 The initiation of fluid seepages and bottom currents, generating fluid escape structures and  
317 palaeo-channels respectively, are documented by the seismic profiles acquired around the  
318 ZCP (Figs.4 – 6). Fluid seepages mainly occurred on the southeast and southwest flanks of  
319 the ZCP at different times. On the southwest flank, fluid escape structures are rooted in strata  
320 older than horizon T30, hence indicating a maximum age of 5.5 Myr (Fig.4). However, on the  
321 southeast flank the fluid escape structures occur below horizon T30 – though lining to the  
322 palaeo-channels and pockmarks buried by the sedimentary stratum younger than T30. This  
323 reveals an onset for pockmarks before 5.5 Myr (Fig.5). In general, present or palaeo  
324 morphologies, including pockmarks and channels, show a close relationship with fluid escape  
325 structures formed by the active fluid seepages. Therefore, the active fluid seepages generated  
326 pockmarks around the ZCP, and the interaction between bottom currents and fluid seepages  
327 led to the maintenance and channelization of these same pockmarks.

328 In summary, we propose that the special and complex morphology around the ZCP results  
329 from the interaction between bottom currents and fluid seepages on the seafloor (Fig.8). The  
330 erosional force of bottom currents was enhanced by active fluid seepages when the bottom  
331 currents flowed across pre-existing or developing pockmarks.

332

## 333 **6. Conclusions**

334 This study shows that the seafloor morphology around the ZCP was reshaped by the  
335 interaction between bottom currents and active fluid seepages. Based on the analysis of high-  
336 resolution bathymetric data and two-dimensional (2D) seismic-reflection data, in this work  
337 we reached the following conclusions:

338 1) A series of alongslope morphological features, such as moats, contourite channels and  
339 drift, have been identified on the seafloor and in some older strata around the ZCP. These  
340 features corroborate the importance of bottom current activities around the ZCP. Moreover, a  
341 large number of pockmarks are identified in the study area, and show a close relationship  
342 with overlying contourite channels.

343 2) Based on the concept of space-for-time substitution, we suggest that the contourite  
344 channels around the ZCP are formed through the coalescence of isolated pockmarks under  
345 the action of bottom currents. The evolution of contourite channels around the ZCP includes  
346 three distinct stages: mature channels (C1, C2, C4 and C5), immature channels (C3, C6 and  
347 C7) and pockmark trails.

348 3) Based on the evolution stages of the contourite channels and their spatial relationship with  
349 seafloor pockmarks, the channels are inferred to develop from north to south. Hence, the  
350 bottom currents around the ZCP are speculated to flow from the north of the ZCP to the  
351 south.

352 4) Active fluid seepages led to the widespread distribution of pockmarks around the ZCP, and  
353 these pre-existed (or developing) pockmarks have significantly contributed to the formation  
354 of contourite channels. The complex bathymetry around ZCP is, therefore, a result of the  
355 interaction between bottom currents and seafloor fluid seepages.



356

357 Fig.8 Three-dimensional conceptual model revealing that bottom current erosion is not the  
358 unique factor leading to the complex seafloor bedforms around the ZCP. Active fluid  
359 seepages induced by post-rift magmatism led to the widespread fluid escape structures and  
360 pockmarks in the surroundings of ZCP (Gao et al., 2019). The pre-existence of the  
361 pockmarks around ZCP are indispensable requirements for the formation of contourite  
362 channels under the erosion of bottom currents. Therefore, the interaction between bottom  
363 currents and active fluid seepages generated the complex bathymetry in the study area, which  
364 comprises moats, contourite channels, contourite drift and pockmarks. The yellow arrows are  
365 proposed pathways for bottom currents in the surroundings of ZCP, and blue arrows indicate  
366 the gravity flows in the Zhongjian canyon. The multibeam bathymetric data are from Lu et al.  
367 (2018).

368

### 369 **Acknowledgements**

370 We thank the PetroChina Hangzhou Research Institute of Geology for the permissions to  
371 release the seismic data. This study was financially supported by the Key Special Project for  
372 Introduced Talents Team of Southern Marine Science and Engineering Guangdong  
373 Laboratory (Guangzhou) (No. GML2019ZD0104), the Guangdong Basic and Applied Basic  
374 Research Foundation (No. 2020B1515020016), the National Natural Science Foundation of  
375 Guangdong Province (No. 2020A1515010497), the National Natural Science Foundation of  
376 China (No. 41876054) and the Guangdong Pearl River Talents Program (No. 2017GC01  
377 0510). Dr. Wei Li is specially funded by the CAS Pioneer Hundred Talents Program  
378 (Y8SL011001). The two anonymous reviewers are thanked for their review and constructive  
379 comments.

380

381 **References**

382 Alves, T. M., 2010. A 3-D morphometric analysis of erosional features in a contourite drift  
383 from offshore SE Brazil. *Geophysical Journal International*, 183: 1151-1164.

384 Andresen, K. J., Huuse, M., and Clausen, O. R., 2008. Morphology and distribution of  
385 Oligocene and Miocene pockmarks in the Danish North Sea – Implications for bottom  
386 current activity and fluid migration. *Basin Research*, 20: 445-466.

387 Bertoni, C., Kirkham, C., Cartwright, J., Hodgson, N., and Rodriguez, K., 2017. Seismic  
388 indicators of focused fluid flow and cross-evaporitic seepages in the eastern Mediterranean.  
389 *Marine and Petroleum Geology*, 88: 472-488.

390 Betzler, C., and Eberli, G. P., 2019. Miocene start of modern carbonate platforms. *Geology*,  
391 47: 771-775.

392 Betzler, C., Brachert, T. C., and Kroon, D., 1995. Role of climate in partial drowning of the  
393 Queensland Plateau carbonate platform (northeastern Australia). *Marine Geology*, 123: 11-  
394 32.

395 Cartwright, J., and Santamarina, C., 2015. Seismic characteristics of fluid escape pipes in  
396 sedimentary basins: Implications for pipe genesis. *Marine and Petroleum Geology*, 65: 126-  
397 140.

398 Chen, H., Xie, X., Zhang, W., Shu, Y., Wang, D., Vandorpe, T., et al., 2016. Deep-water  
399 sedimentary systems and their relationship with bottom currents at the intersection of Xisha  
400 Trough and northwest sub-basin, South China Sea. *Marine Geology*, 378: 101-113.

401 Counts, J. W., Jorry, S. J., Leroux, E., Miramontes, E., and Jouet, G., 2018. Sedimentation  
402 adjacent to atolls and volcano-cored carbonate platforms in the Mozambique Channel (SW  
403 Indian Ocean). *Marine Geology*, 404: 41-59.

404 Courgeon, S., Jorry, S. J., Camoin, G. F., BouDagher-Fadel, M. K., Jouet, G., Révillon, S., et  
405 al., 2016. Growth and demise of Cenozoic isolated carbonate platforms: New insights from  
406 the Mozambique Channel seamounts (SW Indian Ocean). *Marine Geology*, 380: 90-105.

407 de Castro, S., Hernández-Molina, F. J., Rodríguez-Tovar, F. J., Llave, E., Ng, Z. L., Nishida,  
408 N., et al., 2020. Contourites and bottom current reworked sands: Bed facies model and  
409 implications. *Marine Geology*, 428: 106267.

410 de Weger, W., Hernández-Molina, F. J., Flecker, R., Sierro, F. J., Chiarella, D., Krijgsman,  
411 W., et al., 2020. Late Miocene contourite channel system reveals intermittent overflow  
412 behavior. *Geology*, 48: 1194-1199.

413 Dowdeswell, J. A., Evans, J., Cofaigh, C. Ó., and Anderson, J. B., 2006. Morphology and  
414 sedimentary processes on the continental slope off Pine Island Bay, Amundsen Sea, West  
415 Antarctica. *Geological Society of America Bulletin*, 118: 606-619.

416 Eberli, G. P., Anselmetti, F. S., Isern, A. R., and Delius, H., 2010. Timing of changes in sea-  
417 level and currents along Miocene platforms on the Marion Plateau, Australia, Cenozoic  
418 carbonate systems of Australasia. *SEPM Society for Sedimentary Geology Special*  
419 *Publication*, 95: 219-242.

420 Eberli, G. P., Betzler, C., and Frank, T., 2019. Characteristics of modern carbonate contourite  
421 drifts. *Sedimentology*, 66: 1163- 1191.

422 Gao, J., Bangs, N., Wu, S., Cai, G., Han, S., Ma, B., et al., 2019. Post-seafloor spreading  
423 magmatism and associated magmatic hydrothermal systems in the Xisha uplift region,  
424 northwestern South China Sea. *Basin Research*, 31: 688-708.

425 García, M., Hernández-Molina, F. J., Llave, E., Stow, D. A. V., León, R., Fernández-Puga,  
426 M. C., et al., 2009. Contourite erosive features caused by the Mediterranean outflow water in  
427 the Gulf of Cadiz: Quaternary tectonic and oceanographic implications. *Marine Geology*,  
428 257: 24-40.

429 Heinio, P., and Davies, R. J., 2009. Trails of depressions and sediment waves along  
430 submarine channels on the continental margin of Espirito Santo Basin, Brazil. *Geological*  
431 *Society of America Bulletin*, 121: 698-711.

432 Hernández-Molina, F., Larter, R., Rebesco, M., and Maldonado, A., 2006. Miocene reversal  
433 of bottom water flow along the Pacific margin of the Antarctic Peninsula: Stratigraphic  
434 evidence from a contourite sedimentary tail. *Marine Geology*, 228: 93-116.

435 Jackson, C. A. L., Magee, C., and Hunt-Stewart, E. R., 2019. Cenozoic contourites in the  
436 eastern Great Australian Bight, offshore southern Australia: Implications for the onset of the  
437 Leeuwin Current. *Journal of Sedimentary Research*, 89: 199-206.

438 Kilhams, B., McArthur, A., Huuse, M., Ita, E., and Hartley, A., 2011. Enigmatic large-scale  
439 furrows of Miocene to Pliocene age from the central North Sea: Current-scoured pockmarks?  
440 *Geo-Marine Letters*, 31: 437-449.

441 Lei, C., Alves, T. M., Ren, J., and Tong, C., 2020. Rift structure and sediment infill of  
442 hyperextended continental crust: Insights from 3D seismic and well data (Xisha Trough,  
443 South China Sea). *Journal of Geophysical Research: Solid Earth*, 125 (5): e2019JB018610.

444 León, R., Somoza, L., Medialdea, T., Hernández-Molina, F. J., Vázquez, J. T., Díaz-del-Río,  
445 V., et al., 2010. Pockmarks, collapses and blind valleys in the Gulf of Cádiz. *Geo-Marine*  
446 *Letters*, 30: 231-247.

447 Li, C. F., Li, J., Ding, W., Franke, D., Yao, Y., Shi, H., et al., 2015a. Seismic stratigraphy of  
448 the central South China Sea Basin and implications for neotectonics. *Journal of Geophysical*  
449 *Research: Solid Earth*, 120: 1377-1399.

450 Li, W., Alves, T. M., Wu, S., Rebesco, M., Zhao, F., Mi, L., et al., 2016. A giant, submarine  
451 creep zone as a precursor of large-scale slope instability offshore the Dongsha Islands (South  
452 China Sea). *Earth and Planetary Science Letters*, 451: 272-284.

453 Li, W., Alves, T. M., Wu, S., Völker, D., Zhao, F., Mi, L., et al., 2015b. Recurrent slope  
454 failure and submarine channel incision as key factors controlling reservoir potential in the  
455 South China Sea (Qiongdongnan Basin, South Hainan Island). *Marine and Petroleum*  
456 *Geology*, 64: 17-30.

457 Li, W., Krastel, S., Alves, T. M., Urlaub, M., Mehringer, L., Schürer, A., et al., 2018. The  
458 Agadir slide offshore NW Africa: Morphology, emplacement dynamics, and potential  
459 contribution to the Moroccan Turbidite System. *Earth and Planetary Science Letters*, 498:  
460 436-449.

461 Liang, L., Xue, H., and Shu, Y., 2019. The Indonesian Through-flow and the circulation in  
462 the Banda Sea: A modeling study. *Journal of Geophysical Research: Oceans*, 124: 3089-  
463 3106.

464 Liu, Q., Kaneko, A., and Sun, J. L., 2008. Recent progress in studies of the South China Sea  
465 circulation. *Journal of Oceanography*, 64: 753-762.

466 Lu, Y., Li, W., Wu, S., Cronin, B. T., Lyu, F., Wang, B., et al., 2018. Morphology,  
467 architecture, and evolutionary processes of the Zhongjian canyon between two carbonate  
468 platforms, South China Sea. *Interpretation*, 6: SO1-SO15.

469 Lüdmann, T., Kalvelage, C., Betzler, C., Fürstenau, J., and Hübscher, C., 2013. The  
470 Maldives, a giant isolated carbonate platform dominated by bottom currents. *Marine and*  
471 *Petroleum Geology*, 43: 326-340.

472 Menier, D., Pierson, B., Chalabi, A., Ting, K. K., and Pubellier, M., 2014. Morphological  
473 indicators of structural control, relative sea-level fluctuations and platform drowning on  
474 present-day and Miocene carbonate platforms. *Marine and Petroleum Geology*, 58: 776-788.

475 Merino-Tomé, Ó., Porta, G. D., Kenter, J. A. M., Verwer, K., Harris, P. M., Adams, E. W., et  
476 al., 2012. Sequence development in an isolated carbonate platform (lower Jurassic, Djebel  
477 Bou Dahar, High Atlas, Morocco): Influence of tectonics, eustacy and carbonate production.  
478 *Sedimentology*, 59: 118-155.

479 Micallef, A., Ribó, M., Canals, M., Puig, P., Lastras, G., and Tubau, X., 2014. Space-for-time  
480 substitution and the evolution of a submarine canyon-channel system in a passive  
481 progradational margin. *Geomorphology*, 221: 34-50.

482 Michel, J., Laugié, M., Pohl, A., Lanteaume, C., Masse, J. P., Donnadieu, Y., et al., 2019.  
483 Marine carbonate factories: A global model of carbonate platform distribution. *International*  
484 *Journal of Earth Sciences*, 108: 1773-1792.

485 Miramontes, E., Garreau, P., Caillaud, M., Jouet, G., Pellen, R., Hernández-Molina, F. J., et  
486 al., 2019a. Contourite distribution and bottom currents in the NW Mediterranean Sea:  
487 Coupling seafloor geomorphology and hydrodynamic modelling. *Geomorphology*, 333: 43-  
488 60.

489 Miramontes, E., Penven, P., Fierens, R., Droz, L., Toucanne, S., Jorry, S. J., et al., 2019b.  
490 The influence of bottom currents on the Zambezi Valley morphology (Mozambique Channel,  
491 SW Indian Ocean): In situ current observations and hydrodynamic modelling. *Marine*  
492 *Geology*, 410: 42-55.

493 Mulder, T., Ducassou, E., Eberli, G. P., Hanquiez, V., Gonthier, E., Kindler, P., et al., 2012.  
494 New insights into the morphology and sedimentary processes along the western slope of  
495 Great Bahama Bank. *Geology*, 40: 603-606.

496 Mulder, T., Ducassou, E., Hanquiez, V., Principaud, M., Fauquembergue, K., Tournadour, E.,  
497 et al., 2019. Contour current imprints and contourite drifts in the Bahamian Archipelago.  
498 *Sedimentology*, 66: 1192-1221.

499 Mulder, T., Gillet, H., Hanquiez, V., Ducassou, E., Fauquembergue, K., Principaud, M., et  
500 al., 2017. Carbonate slope morphology revealing a giant submarine canyon (Little Bahama  
501 Bank, Bahamas). *Geology*, 46: 31-34.

502 Nolting, A., Zahm, C. K., Kerans, C., and Nikolinakou, M. A., 2018. Effect of carbonate  
503 platform morphology on syndepositional deformation: Insights from numerical modeling.  
504 *Journal of Structural Geology*, 115: 91-102.

505 Pilcher, R., and Argent, J., 2007. Mega-pockmarks and linear pockmark trains on the West  
506 African continental margin. *Marine Geology*, 244: 15-32.

507 Prat, S., Jorry, S. J., Jouet, G., Camoin, G., Vella, C., Le Roy, P., et al., 2016.  
508 Geomorphology and sedimentology of a modern isolated carbonate platform: The Glorieuses  
509 Archipelago, SW Indian Ocean. *Marine Geology*, 380: 272-283.

510 Principaud, M., Mulder, T., Hanquiez, V., Ducassou, E., Eberli, G. P., Chabaud, L., et al.,  
511 2018. Recent morphology and sedimentary processes along the western slope of Great  
512 Bahama Bank (Bahamas). *Sedimentology*, 65: 2088-2116.

513 Principaud, M., Ponte, J. P., Mulder, T., Gillet, H., Robin, C., and Borgomano, J., 2017.  
514 Slope-to-basin stratigraphic evolution of the northwestern Great Bahama Bank (Bahamas)  
515 during the Neogene to Quaternary: Interactions between downslope and bottom currents  
516 deposits. *Basin Research*, 29: 699-724.

517 Purkis, S., Kerr, J., Dempsey, A., Calhoun, A., Metsamaa, L., Riegl, B., et al., 2014. Large-  
518 scale carbonate platform development of Cay Sal Bank, Bahamas, and implications for  
519 associated reef geomorphology. *Geomorphology*, 222: 25-38.

520 Quan, Q., Xue, H., Qin, H., Zeng, X., and Peng, S., 2016. Features and variability of the  
521 South China Sea western boundary current from 1992 to 2011. *Ocean Dynamics*, 66: 795-  
522 810.

523 Rankey, E. C., 2017. Seismic architecture and seismic geomorphology of heterozoan  
524 carbonates: Eocene – Oligocene, Browse basin, northwest shelf, Australia. *Marine and*  
525 *Petroleum Geology*, 82: 424-443.

526 Rebesco, M., Hernández-Molina, F. J., Van Rooij, D., and Wählin, A., 2014. Contourites and  
527 associated sediments controlled by deep-water circulation processes: State-of-the-art and  
528 future considerations. *Marine Geology*, 352: 111-154.

529 Rinke-Hardekopf, L., Reuning, L., Bourget, J., and Back, S., 2018. Syn-sedimentary  
530 deformation as a mechanism for the initiation of submarine gullies on a carbonate platform to  
531 slope transition, Browse Basin, Australian North West Shelf. *Marine and Petroleum Geology*,  
532 91: 622-630.



533 Shao, L., Li, Q., Zhu, W., Zhang, D., Qiao, P., Liu, X., et al., 2017. Neogene carbonate  
534 platform development in the NW South China Sea: Litho-, bio- and chemo-stratigraphic  
535 evidence. *Marine Geology*, 385: 233-243.

536 Stow, D. A. V., Hernández-Molina, F. J., Llave, E., Sayago-Gil, M., Díaz del Río, V., and  
537 Branson, A., 2009. Bedform-velocity matrix: The estimation of bottom current velocity from  
538 bedform observations. *Geology*, 37: 327-330.

539 Surlyk, F., and Lykke-Andersen, H., 2007. Contourite drifts, moats and channels in the upper  
540 Cretaceous chalk of the Danish Basin. *Sedimentology*, 54: 405-422.

541 Tapponnier, P., Lacassin, R., Leloup, P. H., Schärer, U., Dalai, Z., Haiwei, W., et al., 1990.  
542 The Ailao Shan/Red River metamorphic belt: Tertiary left-lateral shear between Indochina  
543 and South China. *Nature*, 343: 431-437.

544 Tian, J., Yang, Q., Liang, X., Xie, L., Hu, D., Wang, F., et al., 2006. Observation of Luzon  
545 Strait transport. *Geophysical Research Letters*, 33: L19607.

546 Velayatham, T., Holford, S. P., and Bunch, M. A., 2018. Ancient fluid flow recorded by  
547 remarkably long, buried pockmark trains observed in 3D seismic data, Exmouth Plateau,  
548 northern Carnarvon Basin. *Marine and Petroleum Geology*, 95: 303-313.

549 Wang, D., Wu, S., Qin, Z., Spence, G., and Lü, F., 2013. Seismic characteristics of the  
550 Huaguang mass transport deposits in the Qiongdongnan Basin, South China Sea: Implications  
551 for regional tectonic activity. *Marine Geology*, 346: 165-182.

552 Wang, L., and Wang, P., 1990. Late Quaternary paleoceanography of the South China Sea:  
553 Glacial-interglacial contrasts in an enclosed basin. *Paleoceanography*, 5: 77-90.

554 Wilson, P. A., Jenkyns, H. C., Elderfield, H., and Larson, R. L., 1998. The paradox of  
555 drowned carbonate platforms and the origin of Cretaceous Pacific guyots. *Nature*, 392: 889-  
556 894.

557 Wu, S., Yang, Z., Wang, D., Lü, F., Lüdmann, T., Fulthorpe, C., et al., 2014. Architecture,  
558 development and geological control of the Xisha carbonate platforms, northwestern South  
559 China Sea. *Marine Geology*, 350: 71-83.

560 Wu, S., Yuan, S., Zhang, G., Ma, Y., Mi, L., and Xu, N., 2009. Seismic characteristics of a  
561 reef carbonate reservoir and implications for hydrocarbon exploration in deepwater of the  
562 Qiongdongnan Basin, northern South China Sea. *Marine and Petroleum Geology*, 26: 817-  
563 823.

564 Wu, S., Zhang, X., Yang, Z., Wu, T., Gao, J., and Wang, D., 2016. Spatial and temporal  
565 evolution of Cenozoic carbonate platforms on the continental margins of the South China  
566 Sea: Response to opening of the ocean basin. *Interpretation*, 4: SP1-SP19.

567 Wunsch, M., Betzler, C., Lindhorst, S., Lüdmann, T., Eberli, G. P., and Della Porta, G., 2017.  
568 Sedimentary dynamics along carbonate slopes (Bahamas archipelago). *Sedimentology*, 64:  
569 631- 657.

570 Yin, S., Hernandez-Molina, F. J., Lin, L., Chen, J., Ding, W., and Li, J., 2021. Isolation of the  
571 South China Sea from the North Pacific Subtropical Gyre since the latest Miocene due to  
572 formation of the Luzon Strait. *Scientific Report*, 11: 1562.

573 Zeng, L., Wang, D., Chen, J., Wang, W., and Chen, R., 2016. SCSPOD14, a South China Sea  
574 physical oceanographic dataset derived from in situ measurements during 1919 – 2014.  
575 *Scientific Data*, 3: 160029.

576 Zhang, C., Sun, Z., Manatschal, G., Pang, X., Qiu, N., Su, M., et al., 2021. Syn-rift magmatic  
577 characteristics and evolution at a sediment-rich margin: Insights from high-resolution seismic  
578 data from the South China Sea. *Gondwana Research*, 91: 81-96.

579 Zhao, F., Alves, T. M., Xia, S., Li, W., Wang, L., Mi, L., et al., 2020. Along-strike  
580 segmentation of the South China Sea margin imposed by inherited pre-rift basement  
581 structures. *Earth and Planetary Science Letters*, 530: 115862.

582 Zhou, D., Ru, K., and Chen, H. Z., 1995. Kinematics of Cenozoic extension on the South  
583 China Sea continental margin and its implications for the tectonic evolution of the region.  
584 *Tectonophysics*, 251: 161-177.

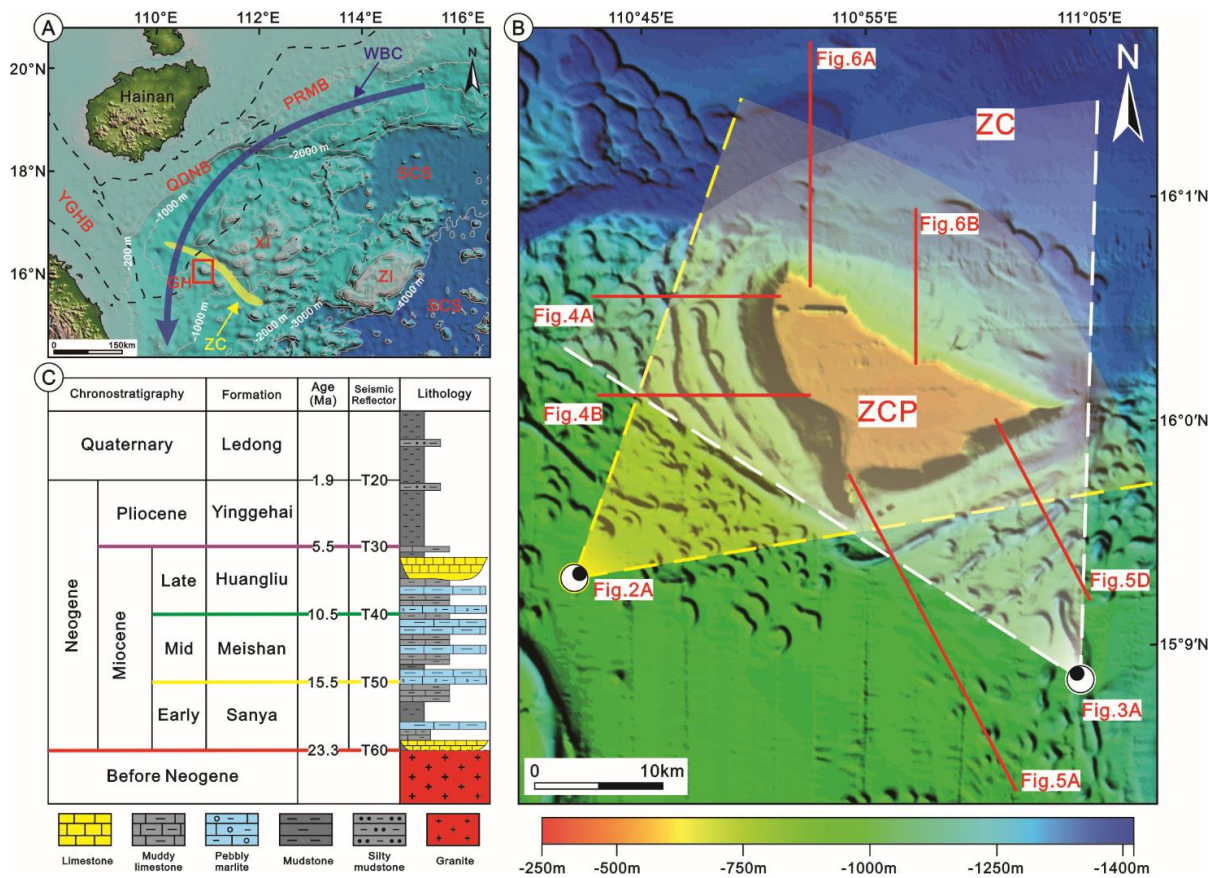
585 Zhu, W., Xie, X., Wang, Z., Zhang, D., Zhang, C., Cao, L., et al., 2017. New insights on the  
586 origin of the basement of the Xisha uplift, South China Sea. *Science China (Earth Sciences)*,  
587 60: 2214-2222.

588 Zhu, Y., Sun, J., Wang, Y., Li, S., Xu, T., Wei, Z., et al., 2019. Overview of the multi-layer  
589 circulation in the South China Sea. *Progress in Oceanography*, 175: 171-182.

590

591

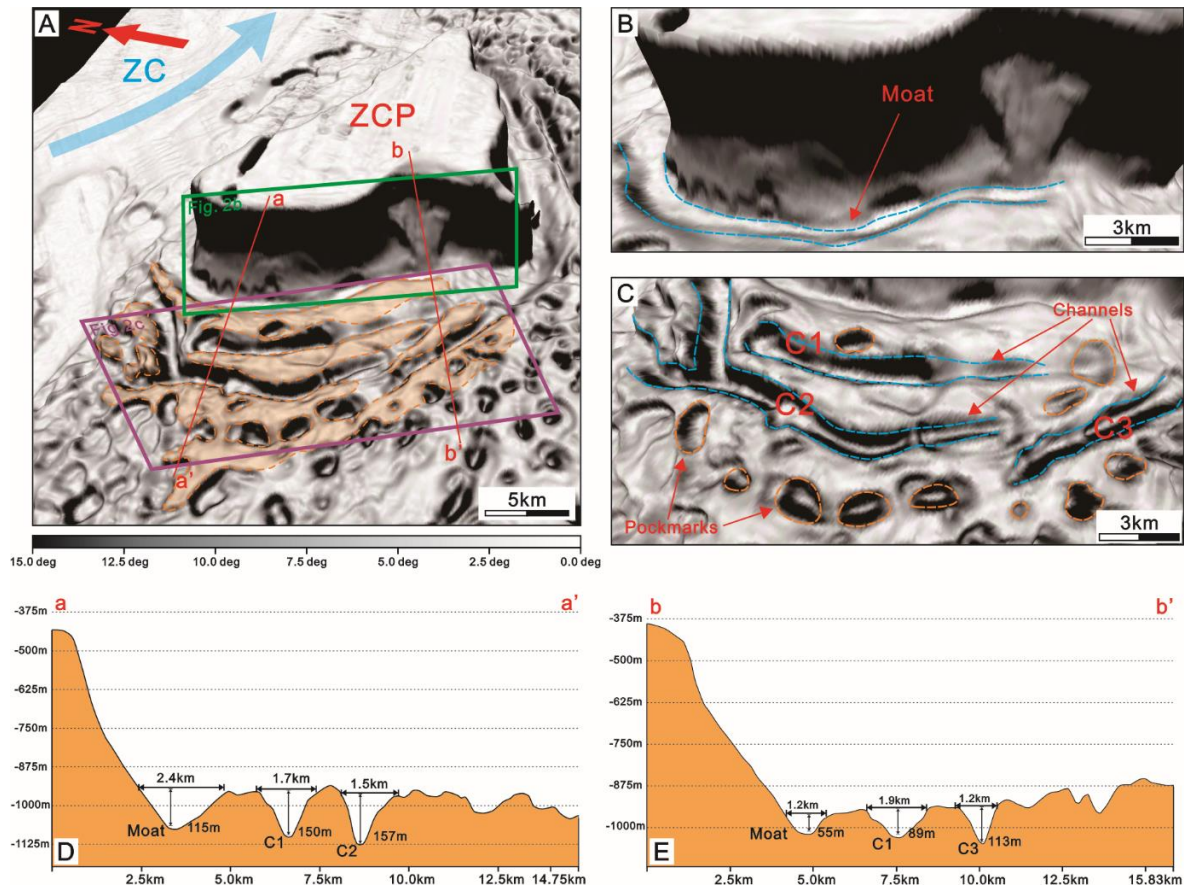
592 **Figures**



593

594 Fig.1 A) Regional geological setting of the study area. Modified from Gao *et al.* (2019).  
 595 Black dashed lines indicate the boundaries of sedimentary basins in the Northwest South  
 596 China Sea. The dark blue curve arrow indicates the Western Boundary Currents (WBC) of  
 597 South China Sea, and the yellow belt shows the layout of Zhongjian canyon (ZC). The red  
 598 box indicates the location of study area shown as Fig.1B. B) Multibeam bathymetric map of  
 599 the study area (modified after Lu *et al.* (2018)). The Zhongjianbei carbonate platform (ZCP)  
 600 is located at the very center of the study area, next to the Zhongjian canyon (ZC) in the  
 601 northeast. Red solid lines indicate the locations of two-dimensional seismic profiles  
 602 acquired in the vicinity of the ZCP, and the ‘eye’ symbols combined with yellow and white  
 603 dashed lines indicate the viewpoints of Fig.2A and Fig.3A respectively. C) Stratigraphic  
 604 column of the study area based on Lu *et al.* (2018) and Gao *et al.* (2019). Key: YGH,  
 605 Yinggehai Basin; QDNB, Qiongdongnan Basin; PRMB, Pearl River Mouth Basin; XI,  
 606 Xisha Islands; ZI, Zhongsha Islands; GH, Guangle high; SCS, South China Sea.

607

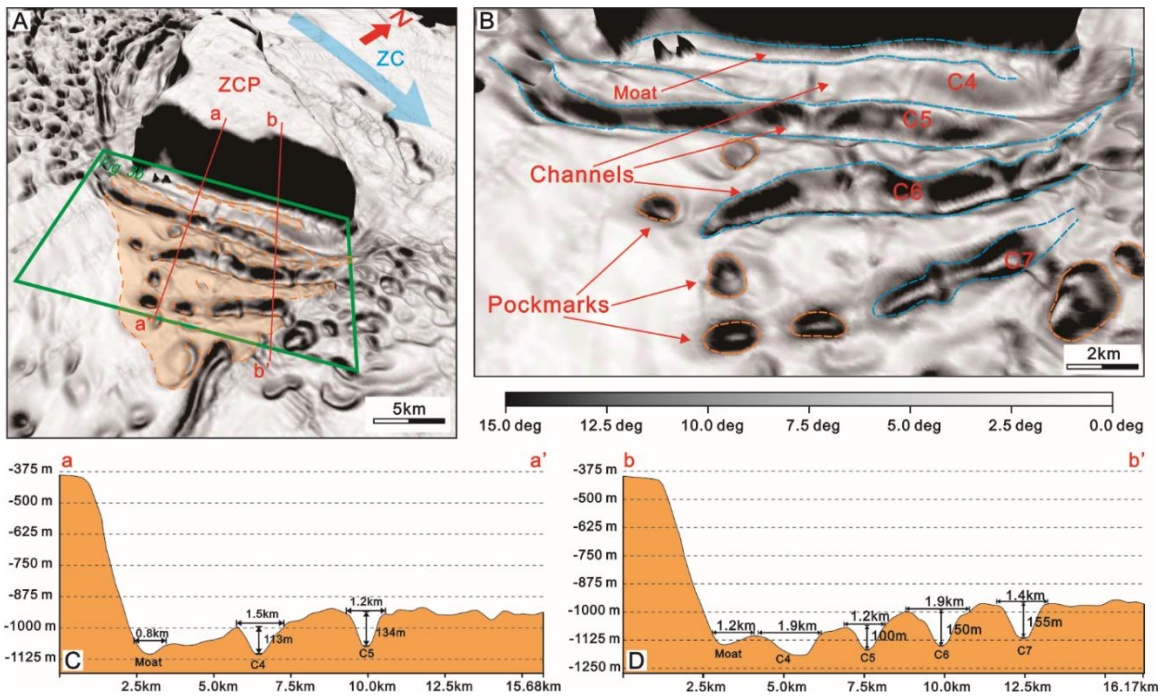


608

609 Fig.2 A) Three-dimensional slope gradient map depicting a southwest view of the ZCP with  
 610 the viewpoint shown in Fig.1B. Blue solid arrow indicates the direction of gravity flows in  
 611 the ZC. Orange dashed lines highlight the features associated with alongslope currents. Red  
 612 solid lines indicate the locations of bathymetric profiles (shown in Figs.2D and 2E) across the  
 613 platform slope and associated channel-like erosional features. The multibeam bathymetric  
 614 data for morphological description is from Lu et al. (2018). B) Moat along the flanks of the  
 615 ZCP. C) Details of three channels (C1, C2 and C3) formed in the southwest flanks of ZCP,  
 616 which are sub-parallel to the moat. Numerous pockmarks are observed around these channels.  
 617 D) and E) Bathymetric profiles revealing the cross-section geometries (width and depth of  
 618 incision) of the moat and channels.

619

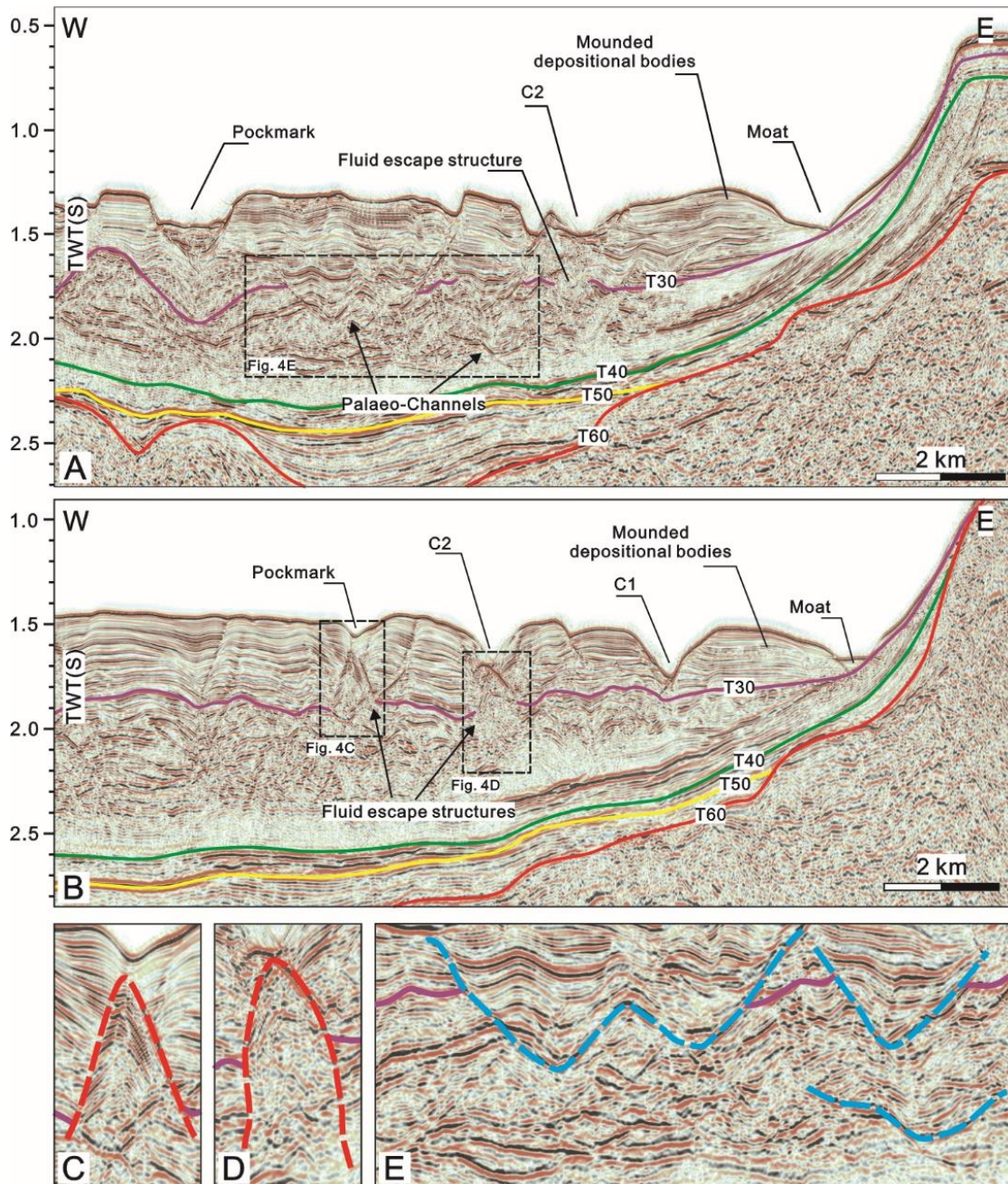




620

621 Fig.3 A) Slope gradient map revealing the three-dimensional morphology of the southeast  
 622 flank of the ZCP. The features associated with alongslope processes are indicated by orange  
 623 dashed lines. In the ZC, gravity flows to the southeast direction are indicated by the blue  
 624 arrow. Red solid lines show the distribution of the bathymetric profiles crossing the platform  
 625 flanks, moat and channels. The viewpoint of Fig.3A is shown in Fig.1B. B) Four channels  
 626 (C4, C5, C6 and C7) are identified in the southeast flank of the ZCP. They are sub-parallel to  
 627 the observed moat and surrounded by pockmarks. C) and D) Bathymetric profiles (a – a’ and  
 628 b – b’ in Fig.3A) showing the U-shaped cross-sections, width and incision depth of moat and  
 629 channels. The bathymetry is after Lu et al. (2018).

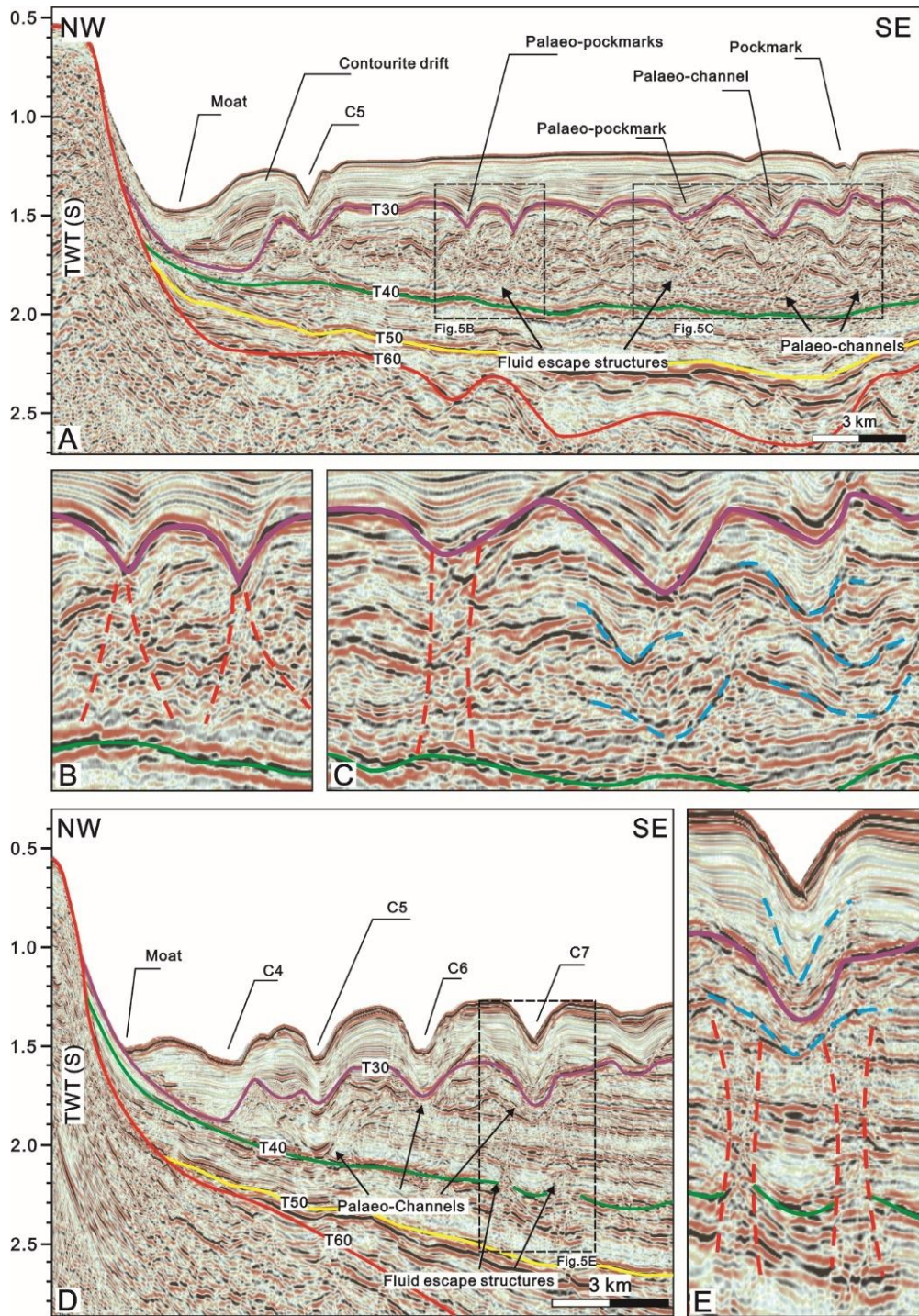
630



631

632 Fig.4 A) and B) Seismic profiles imaging the sub-seafloor strata in the southwest flank of the  
 633 ZCP and associated erosional and depositional features. Stratigraphic horizons T60, T50, T40  
 634 and T30 and sub-surface structures are also illustrated. The locations of the seismic profiles  
 635 are shown in Fig.1B. The seismic data is after Wang et al. (2013) and Wu et al. (2014). C)  
 636 and D) Zoomed-in seismic profile showing the fluid escape structures (depicted by red  
 637 dashed lines) cross Horizon T30 (shown as purple solid line) and their link with the  
 638 depressions on the seafloor. E) Zoomed-in seismic section revealing the presence of palaeo-  
 639 channels (shown as blue dashed lines), which truncate or underlie the Horizon T30 (purple  
 640 solid lines).





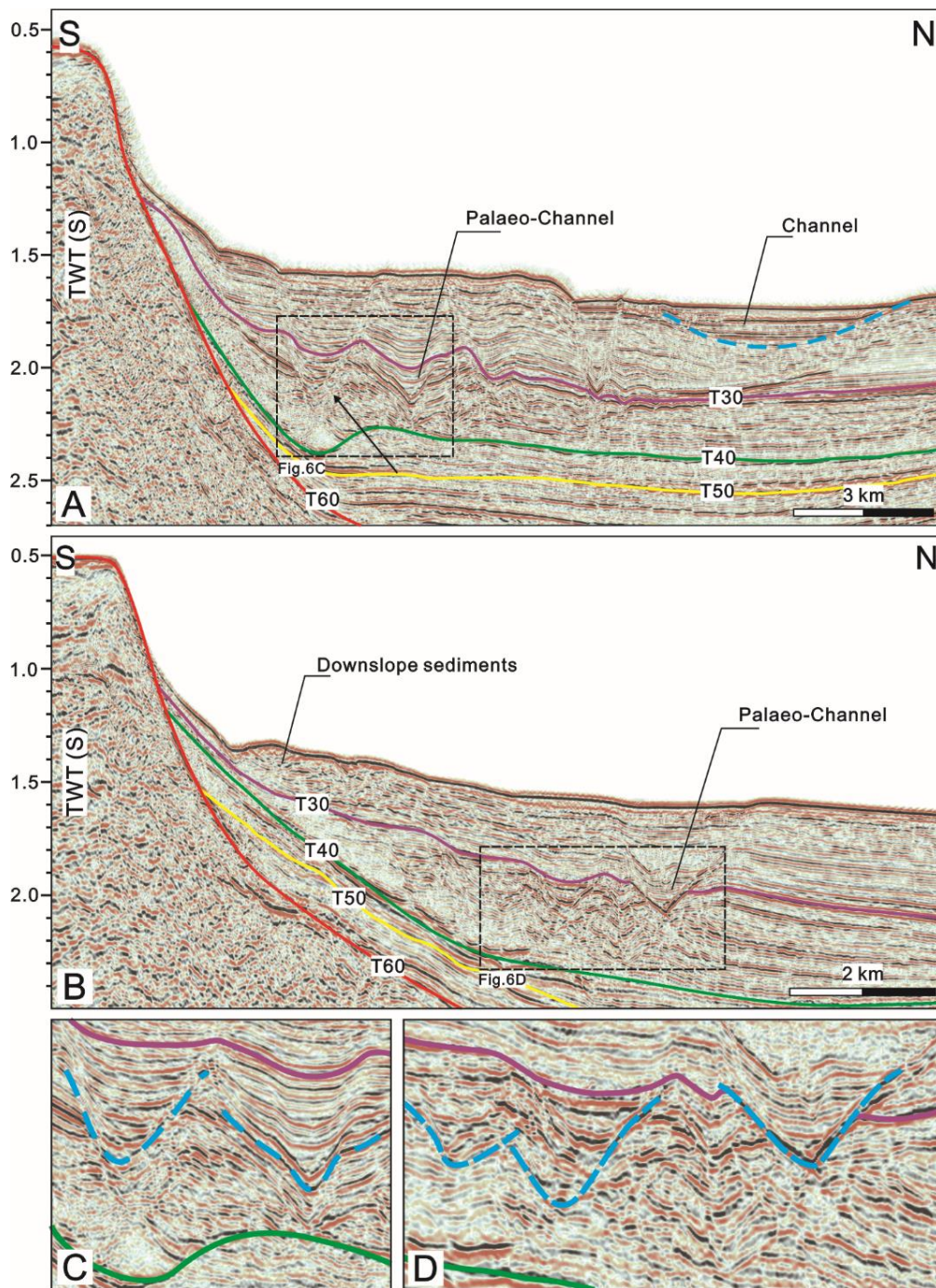
642

643 Fig.5 A) Seismic profile highlighting the multiple seafloor features and structures in the  
 644 southeast flank of the ZCP (see location in Fig.1B). Moats, channels, pockmarks and  
 645 contourite drifts are identified on the seafloor. Palaeo-channel, palaeo- pockmarks and fluid  
 646 escape structures are observed in older strata. B) Zoomed-in seismic profile showing the  
 647 relationship between fluid escape structures (outlined by red dashed lines) and palaeo-



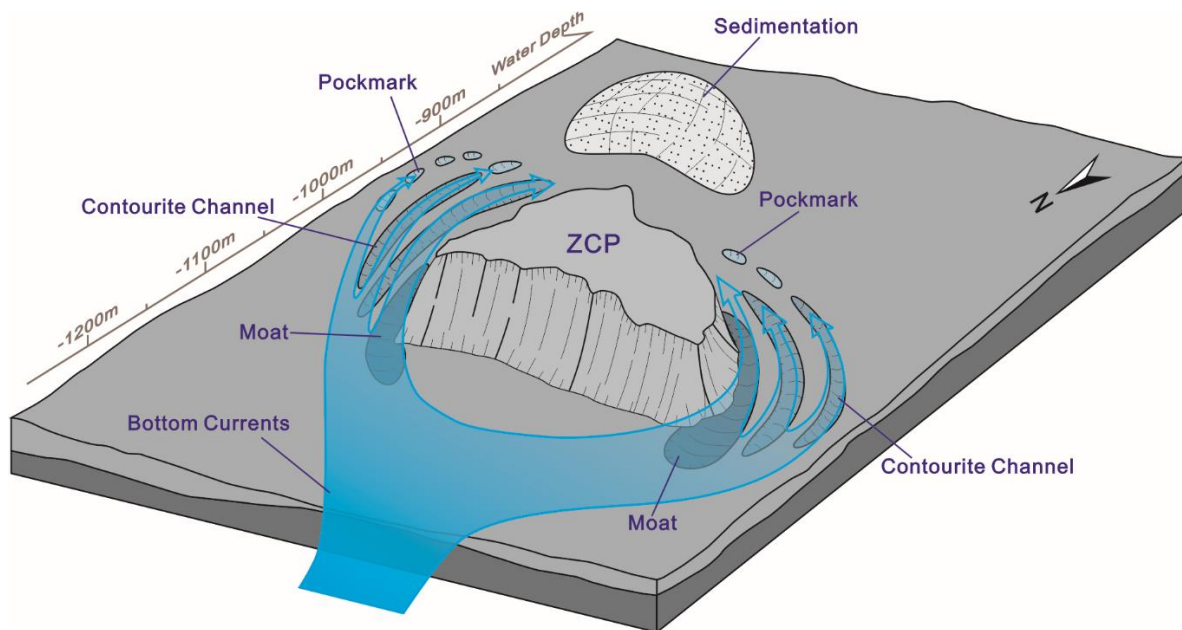
648 pockmarks. Purple and green solid lines represent seismic reflection T30 and T40,  
649 respectively. C) Zoomed-in seismic profile revealing that the migration of palaeo-channels  
650 (shown as blue dashed lines) and palaeo-pockmarks is associated with fluid escape features  
651 (depicted as red dashed lines). D) Seismic profile showing subsurface structures and the  
652 seafloor bathymetry, including moat and channels (C4, C5, C6 and C7) on the southeast flank  
653 of the ZCP. E) Zoomed-in seismic profile revealing the spatial relationship between modern  
654 channels, palaeo-channels (shown as blue dashed lines), fluid escape features (outlined by red  
655 dashed lines) and Horizon T40 (shown as green solid lines). The original seismic profiles are  
656 from Wang et al. (2013) and Wu et al. (2014).

657



659

660 Fig.6 A) and B) Seismic profiles imaging the northeast flank of the ZCP. The blue dashed  
 661 line indicates a buried channel close to the seafloor. The locations of seismic profiles are  
 662 shown in Fig.1B. C) and D) Zoomed-in seismic profiles showing the palaeo-channels (shown  
 663 as blue dashed lines) in strata beneath Horizon T30. Purple and green solid lines indicate  
 664 Horizons T30 and T40, respectively. The interpretation is based on the original seismic data  
 665 after Wang et al. (2013) and Wu et al. (2014).



666

667 Fig.7 Sketch summarizing the pathways of bottom currents around the ZCP and how  
 668 seafloor morphology influences the dynamics of bottom currents. In the study area, the  
 669 bottom currents are proposed to flow from the north and to the south, and split by the obstacle  
 670 of ZCP. The existence of obstacle has led to the enhancement of bottom current erosion on  
 671 the south flanks of platform, especially close to the slope bottom of ZCP. Therefore, on the  
 672 flanks of ZCP, the erosional moats were formed at the bottom of slopes and pockmark trails  
 673 are involved into contourite channels under the bottom current erosion. Furthermore, due to  
 674 the long-distance (tens of kilometres) upslope transportation (from north to south), the  
 675 sediment transport capacity of bottom currents has significantly decreased. The suspending  
 676 sediments carried by bottom currents hence deposited at the south region of ZCP, which is  
 677 covered by a large area of smooth seafloor with rare erosional features.

678